


Phonon resonance effect and defect scattering in covalently bonded carbon nanotube networks

Xiguang Wu,¹ Yajuan Cheng,² Shaoming Huang,¹ and Shiyun Xiong^{1,*}

¹Guangzhou Key Laboratory of Low-Dimensional Materials and Energy Storage Devices, School of Materials and Energy, Guangdong University of Technology, Guangzhou 510006, China

²School of Physics and Materials Science, Guangzhou University, Guangzhou 510006, China

 (Received 11 May 2024; revised 20 July 2024; accepted 25 July 2024; published 13 August 2024)

Covalently bonded carbon nanotube (CNT) networks offer promising potential for heat-dissipation applications due to their low interfacial thermal resistivity between connected CNTs. In this work, the thermal-transport properties of covalently bonded CNT networks were simulated by molecular dynamics. It was found that the thermal conductivity (TC) of the networked CNTs is periodic dependent. Although the TCs are reduced compared to those of pristine CNTs, they are considerably larger than the values in thermal interface materials. The TC reduction with respect to the pristine CNTs primarily stems from defect scattering at junctions and resonant scattering generated by CNTs oriented perpendicular to the transport direction. The two mechanisms operate over different frequency ranges and collectively contribute to a reduction in both phonon group velocity and relaxation time across the entire frequency range. Moreover, we demonstrate that increasing the network period in a specific direction increases the TC along this direction, while reduces TC in the perpendicular direction due to intensified resonant coupling. Such directional-dependent TC variations with period facilitate the regulation of thermal-transport anisotropy within CNT networks. Overall, our findings elucidate the underlying phonon transport mechanisms in CNT networks and offer valuable insights into the design of thermal interface materials, thermal insulation materials, and materials with tailored thermal anisotropy. By leveraging the identified mechanisms, it becomes possible to develop CNT-based materials with enhanced heat-dissipation capabilities and engineered TC profiles.

DOI: [10.1103/PhysRevApplied.22.024038](https://doi.org/10.1103/PhysRevApplied.22.024038)

I. INTRODUCTION

Owing to their exceptional thermal conductivity (TC) and mechanical stability, carbon nanotubes (CNTs) are widely utilized in nanoelectronic devices and thermal management materials, such as nanosensors [1–3] and flexible electronics [4,5] to nanocomposites [6–9] and heat-dissipation materials [10–14]. In the realm of heat-dissipation materials, CNTs are commonly incorporated as additives into a polymer matrix to create thermal conductive pathways, which could significantly enhance the polymer's TC. The degree of enhancement can range from 7 to 50 times, depending on the loading concentration of CNTs [15–17]. However, the quasi-one-dimensional structure of CNTs, coupled with weak van der Waals interactions between CNT and CNT, and CNT and polymers, introduce significant thermal resistance. Consequently, CNTs can only form local thermal conductive channels rather than a comprehensive conductive network. This limitation

restricts their effectiveness in enhancing the TC of thermal interface materials.

To overcome this limitation, researchers commonly employ surface-modification techniques for CNTs or introduce functional groups in polymers, such as carboxyl, hydroxyl, and amino groups. This approach facilitates the formation of covalent bonds between CNTs and functional groups, thereby improving the interactions between CNTs and polymers through such bridging. By doing so, the vibrational density of states (DOS) compatibility between CNTs and the polymer is enhanced, resulting in a reduction of interfacial thermal resistance and an overall enhancement of TC. For example, Ni *et al.* demonstrated a considerable reduction in interfacial thermal resistance between HLK5 molecules and CNTs, from 1.5 to 0.34 mm² KW⁻¹, after the formation of covalent bonds [18]. Chen *et al.* observed an enhancement in the effective TC of polymers from 0.22 to 0.37 Wm⁻¹ K⁻¹, by incorporating 0.8% (by volume) of hydroxyl-functionalized single-walled CNTs. In contrast, the addition of pristine CNTs resulted in a more modest increase, achieving a TC of only 0.29 Wm⁻¹ K⁻¹ [19]. Similarly, Tian *et al.*

*Contact author: syxiong@gdut.edu.cn, xiongshiyun216@163.com

reported increases in the TC of CNT-containing nanofluid by 11.49% and 4.72% after modifying CNT with hydroxyl and carboxyl groups, respectively, at a concentration of 2.0 wt% [20].

Recent advancements have enabled the synthesis of CNT network structures with covalent bonds [21,22], resulting in the formation of configurations such as X , Y , and T junctions [23,24]. These experiments serve as a crucial reference for optimizing the synthesis technology of periodically arranged CNT junctions. These bonded structures exhibit significantly reduced thermal resistance between individual CNTs and hold great potential for advanced thermal-management applications. Covalently bonded CNT networks with varying tube diameters have also shown thermal rectification properties [25,26]. The synthesis of such covalently bonded CNT structures provides a foundation for more intricate network designs [27], which can expand the application of CNTs, particularly in the field of thermal dissipation. Furthermore, these networked CNT structures show promise in various applications, including highly sensitive strain sensors [3], hydrogen storage [28], multiterminal charge-transport media [29], and nanoelectronic circuits [30].

Connecting CNTs through covalent bonds provides a robust solution to overcome the high interfacial thermal resistance associated with van der Waals interactions, which facilitates the formation of thermally conductive networks in three dimensions. Such bonding leads to the creation of thermally conductive networks extending across three-dimensional (3D) spaces when dispersed in organic thermal interface materials, and thus could significantly enhance thermal-transport and heat-dissipation capabilities. To optimize covalently bonded CNT networks for thermal-management applications, it is crucial to understand their thermal-transport properties in detail. Utilizing molecular dynamics simulations, Varshney *et al.* found that the 3D CNT network structures exhibit a reduced TC compared to pristine CNTs. Notably, they discovered that by adjusting the spacing of the junctions, it is possible to modulate the TC of the networks [31].

In this paper, we explore the thermal-transport properties of CNT networks using homogeneous nonequilibrium molecular dynamics (HNEMD) simulations. Various network structures ranging from one-dimensional (1D) branched structures to two-dimensional (2D) and 3D networks were examined. It was demonstrated that these CNT networks exhibited two key phenomena: phonon scattering and phonon-resonance effects. These phenomena collectively contribute to a substantial reduction in TC compared to pristine CNTs across the entire frequency ranges. Furthermore, we highlight tunability of TC by manipulating the network period both parallel and perpendicular to the transport direction. Our results demonstrate that the TC increases with the period parallel to the transport direction, while decreases with the period perpendicular to the

transport direction. This anisotropic behavior provides a strategy to fine tune the thermal-transport properties of CNT networks, providing strategic insights for the design of advanced thermal-management systems. Overall, our research sheds light on the complex thermal-transport behavior of CNT networks and highlights the potential for tailoring their thermal properties by controlling the network structure. Such knowledge is valuable for the development of advanced thermal-management systems that require precise control over TC.

II. STRUCTURE AND SIMULATION METHOD

In our simulation, we first constructed branched 1D CNT models with covalent bonds. These models included configurations such as (16,0)–(16,0), (10,10)–(10,10), and (10,10)–(8,8) where the numbers in parentheses denoted the chirality of the main-chain CNTs and the branched CNTs [as shown in Fig. 1(a)]. The height of the branched CNT was denoted as L_h , and the distance between adjacent branches (i.e., period) was denoted as L_m . We extended this framework to develop 2D and 3D CNT network models based on (10,10) CNTs [Figs. 1(b) and 1(c)]. The periods of the network along the x , y , and z axes were represented by L_x , L_y , and L_z , respectively. In the intersection regions of the CNTs, carbon rings deviate from hexagonal were formed, including pentagonal (m_5), heptagonal (m_7), and octagonal (m_8) configurations [Fig. 1(a)]. These arrangements satisfied Euler's polyhedron formula:

$$2m_8 + m_7 - m_5 = G, \quad (1)$$

where G equals 12 for 1D and 2D models, and 24 for 3D models [32].

By utilizing these models and configurations, we were able to investigate the thermal-transport properties of the CNT networks and explore their behavior in relation to the geometrical parameters, such as branch height and period in different dimensions.

All simulations were performed using the GPUMD package [33]. The Tersoff potential [34] was used to describe the interactions of the C—C covalent bonds. The velocity-Verlet algorithm with a timestep of 0.5 fs was employed to integrate the equations of motion during the simulations. The TC of 1D, 2D, and 3D networks were calculated independently with the HNEMD method [35]. Prior to data collection, each structure was equilibrated in the NVT ensemble at a temperature of 300 K for a duration of 2 ns. The temperature during the equilibration process was controlled using the Nosé-Hoover chain thermostat [36]. Following the structural equilibration, HNEMD simulations were performed for a duration of 10 ns (20 ns for 1D structures) to evaluate TC, and the final TC were averaged by the results from three independent simulations. The HNEMD method allows for spectral decomposition

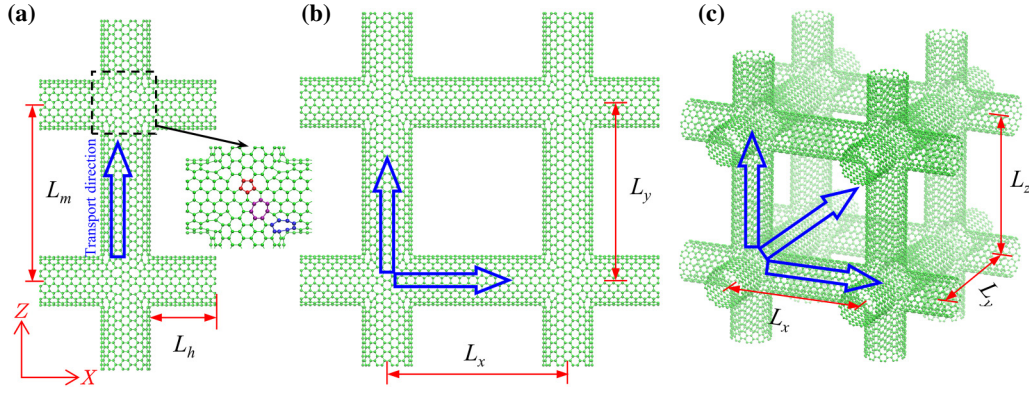


FIG. 1. Schematic representation of covalently bonded CNT structures. (a) A 1D CNT showing a branched morphology with designated branch heights (L_h) and periods (L_m). The offside panel highlights an example of pentagonal, heptagonal, and octagonal rings in the junctions. (b) A 2D network constructed from interconnected CNTs, illustrating the periodicity in the x and y axes (L_x and L_y). (c) A 3D CNT network, highlighting the periodic junctions in the x , y , and z axes (L_x , L_y , and L_z). In all systems, periodic boundary conditions were used in the transport direction while free-boundary conditions were applied in other directions.

of TC [35]:

$$\kappa(\omega) = \frac{2}{TVF_e} \int_{-\infty}^{\infty} dt e^{i\omega t} K(t), \quad (2)$$

where T and V are the temperature and volume of the system, respectively; F_e is the external driving force; $K(t) = \sum_i \langle W_i(0) \cdot v_i(t) \rangle$ is the force-velocity correlation function with W_i and v_i being the potential force tensor and velocity of atom i , respectively. After obtaining the spectral TC, we could further calculate the phonon mean free path (MFP) of the system:

$$\lambda(\omega) = \frac{\kappa(\omega)}{G(\omega)}, \quad (3)$$

where $G(\omega)$ is the spectral thermal conductance in the ballistic limit, which can be calculated based on the nonequilibrium molecular dynamics (NEMD) simulations [37–39].

It is worthwhile to note that we did not apply quantum corrections to the TC results obtained from our MD simulations. Despite the development of methods to incorporate quantum corrections, such as the temperature-scaling method and the spectral correction method, fully accounting for quantum effects in TC calculations remains a significant challenge [40]. The classical approach tends to overestimate the population of high-frequency phonons. Although this results in some discrepancies in the predicted TCs, these discrepancies are relatively minor due to the short phonon mean free paths beyond 3 THz in covalently bonded structures, as illustrated in Figs. 4 and 7. For these reasons, we chose not to consider quantum corrections in our study.

III. RESULTS AND DISCUSSION

In our investigation, the thermal-transport properties of 1D branched CNTs with covalent bonds were analyzed firstly. Three specific structures including (16,0)–(16,0), (10,10)–(10,10), and (10,10)–(8,8) were examined. The (16,0)–(16,0) structure consisted of zigzag chirality for both the main and branched CNTs, while the (10,10)–(10,10) and (10,10)–(8,8) structures comprised armchair CNTs, with the latter having a reduced diameter for the branched CNT. For comparison, we calculated the TC of pristine (16,0) and (10,10) CNTs, obtaining values of 2250 ± 83 and $2170 \pm 42 \text{ Wm}^{-1} \text{ K}^{-1}$, respectively. These results were close to the results reported in the literature [35]. In the case of the branched CNTs with covalent bonds, we observed a significant decrease in TC [Fig. 2(a)]. This reduction could be attributed to two main factors: intense phonon scattering at covalently bonded junctions and the presence of phonon resonance resulting from the branched structures. Defects at the junctions of the branched CNTs caused pronounced scattering of phonons, particularly affecting high-frequency phonons [41]. On the other hand, the discontinuous side branches, oriented perpendicular to the main CNT, facilitated the formation of standing-wave resonant modes. These resonant modes interacted with propagating phonons in the main CNT, effectively reducing their group velocity and relaxation time. This phonon resonant effect was most pronounced for low-frequency, long-wavelength phonons, providing a complementary mechanism to defect scattering in reducing TC [42–44].

Figure 2(a) illustrates the TC for the three types of branched CNTs (1D structure) mentioned earlier with varying branching period L_m , while keeping the height of the branched CNT fixed at 1.8 nm. Among the studied 1D structures, the (10,10)–(10,10) CNT configuration

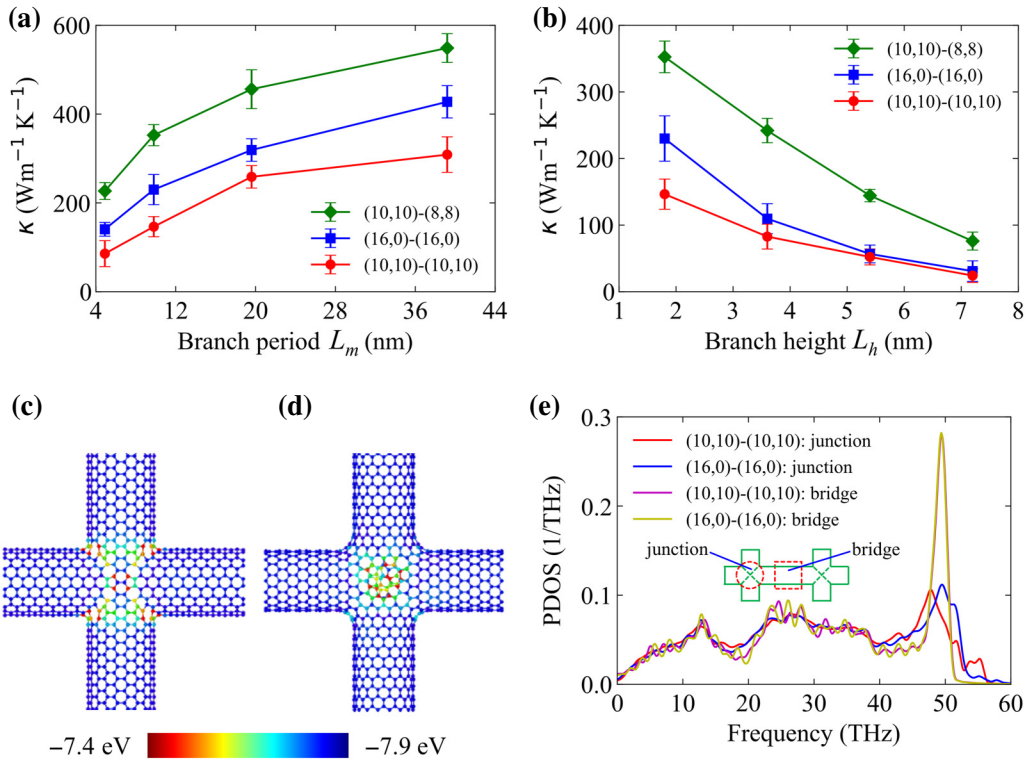


FIG. 2. Variation of TC in 1D branched CNTs with the period length (a) and branch height (b); atomic energy distributions of (10,10)–(10,10) branched CNT (c) and (16,0)–(16,0) branched CNT (d); (e) phonon DOS for atoms at junctions and away from junctions in (10,10)–(10,10) and (16,0)–(16,0) branched CNTs.

exhibited the lowest TC, while the (10,10)–(8,8) CNT displayed the largest TC. This finding highlights the significant influence of chirality and diameter of branched CNTs on thermal transport. All systems demonstrated an increase in TC as the branching period of the CNTs increased, attributing to the reduced density of defects and resonant structures. Notably, when the side-chain spacing was set at 4.9 nm, the TC of the branched (16,0)–(16,0), (10,10)–(10,10), and (10,10)–(8,8) structures was reduced by 93.7%, 96.0%, and 89.6%, respectively, compared to their pristine counterparts. This significant reduction in TC highlights the impact of covalently bonded side branches on the thermal transport of 1D CNTs. The large difference in TC between the (10,10)–(10,10) and (10,10)–(8,8) 1D structures suggests that the diameter of the branched CNTs can be used to tune and manipulate TC in branched CNT structures. In addition, we investigated the variation of TC with the height of branched CNTs [Fig. 2(b)]. It was observed that TC decreased across all three systems as the height of branched CNTs increased. Furthermore, the disparities in TC among the three systems diminished with increasing height. As increasing the height of the branched CNTs does not affect the defects at the junctions, it signifies that the branched CNT height influences TC exclusively through the phonon-resonance effect by modifying the number and frequency of the resonant phonons [44].

The bonding alterations at the junctions of the main and branched CNTs result in the formation of carbon ring structures with five, seven, and eight members in addition to the normal six-member rings. These alterations have a significant impact on the local atomic energies, as evidenced by the atomic potential energy maps in Figs. 2(c) and 2(d). The energies of atoms in the main chain and branched CNTs away from junctions are basically the same. However, at the junctions, the atomic energies are significantly elevated. Notably, the distribution of atomic energy differs between the 1D(10,10)–(10,10) and 1D (16,0)–(16,0) structures. In the former, atoms with higher energies are concentrated at the geometric intersection line of the main and branched CNTs, while in the latter, atoms in the central region of the junctions exhibit higher energies. These variations in atomic energies at the junctions induce different stress levels, which further alter atomic vibrational characteristics. This is illustrated by the vibrational DOS for atoms located on the junctions and away from the junctions [notated as bridges, see Fig. 2(e)] in both the (10,10)–(10,10) and (16,0)–(16,0) structures [Fig. 2(e)]. The vibrational DOS curves for atoms at bridges in (10,10)–(10,10) and (16,0)–(16,0) structures are similar. While the vibrational DOS at the junctions for both structures differs from that at bridges, particularly above 40 THz, where the DOS peaks at junctions in both

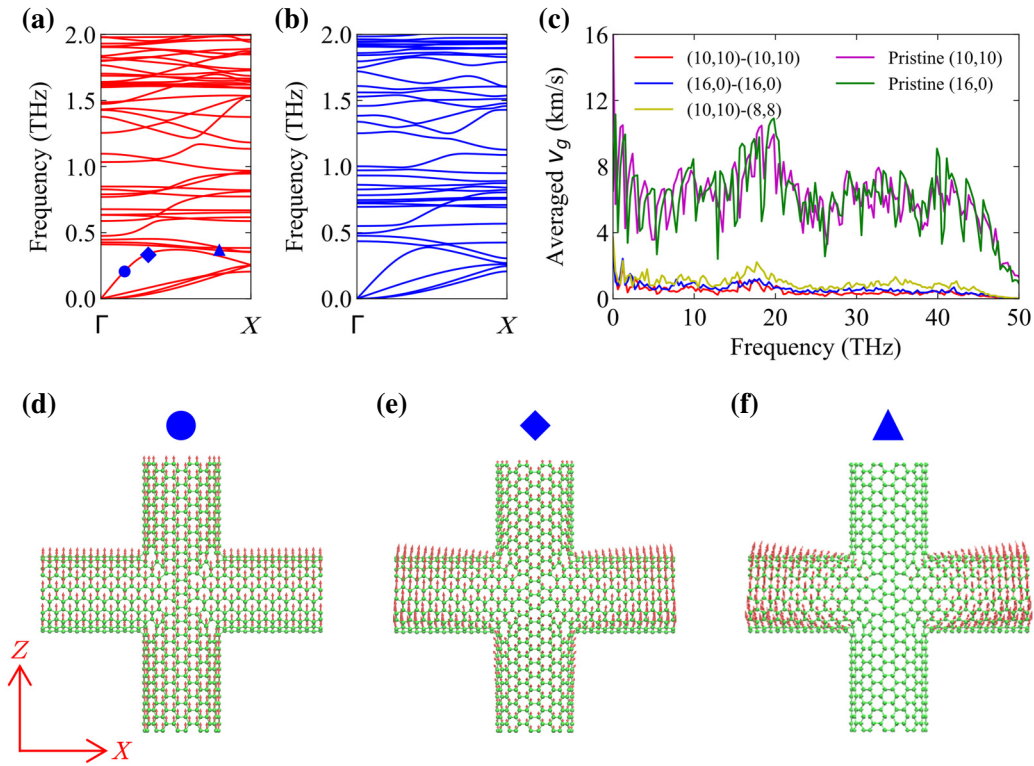


FIG. 3. Phonon-dispersion curves of (10,10)–(10,10) branched CNT (a) and (16,0)–(16,0) branched CNT (b) at 0–2 THz; (c) average phonon group velocities as a function of frequency in different 1D CNT systems; visualization of phonon eigenvectors for the modes marked in the dispersion curve: circles (d), diamond (e), and triangle (f). Here the z direction is periodic and it corresponds to the transport direction. The period and branch height are $L_m = 4.9$ nm and $L_h = 1.8$ nm, respectively.

systems are significantly weakened. In the (10,10)–(10,10) structure, additional vibrational peaks emerge between 52–56 THz, and a red shift for the peak at 49 THz is observed compared to the original peaks. Compared to the 1D (16,0)–(16,0) structure, the larger deviation of the DOS for the 1D (10,10)–(10,10) structure results in a smaller DOS overlap between atoms at the junctions and bridges. Consequently, the scattering of phonons by the junctions in the (10,10)–(10,10) structure is stronger, which partially accounts for the lower TC observed.

To further investigate the phonon properties in the branched 1D CNTs, we calculated the phonon-dispersion curves using the GULP software [45]. Figures 3(a) and 3(b) display the phonon-dispersion curves for 1D (10,10)–(10,10) and 1D (16,0)–(16,0) CNT structures with $L_m = 4.9$ nm and $L_h = 1.8$ nm. A comparison with the dispersion of pristine CNTs reveals the emergence of numerous flat bands with group velocities close to zero in both the (10,10)–(10,10) and (16,0)–(16,0) CNTs. These flat bands are indicative of resonance modes within the branched structures. Notably, these resonant phonons in the branched CNTs not only possess minimal group velocity but also engage in hybridization with propagating phonons in the main CNT. This hybridization, stemming from the band anticrossing effect, leads to a reduction

in the group velocity of the propagating phonons as shown in Fig. 2(e). Pristine structures, such as (16,0) and (10,10) CNTs, exhibit similar group velocities. However, the branched structures exhibit a significant reduction in group velocity across the entire frequency range compared to their corresponding pristine CNTs. The magnitude of this reduction aligns with the relative TC of the three structures.

To visualize the coupling between resonant and propagating phonons, we calculated phonon eigenvectors for the 1D (10,10)–(10,10) CNT. Figures 3(d)–3(f) illustrate the eigenvector evolution from a pure longitudinal acoustic phonon to a pure resonant mode [marked by circles, squares, and triangles in Fig. 3(a)]. When examining phonons located far from the flat band (circles), the phonon exhibits vibrational characteristics of the longitudinal acoustic phonon, with all atoms vibrating at the same amplitude along the transport direction. However, within the flat bands (triangles), the modes localize almost exclusively in the branched CNTs, which is consistent with the characterization of the resonant modes. In the vicinity of the flat band (squares), atomic vibrations reflect a superposition of resonant mode and longitudinal acoustic mode, providing evidence of the hybridization between these two modes. This hybridization leads to a flattened dispersion

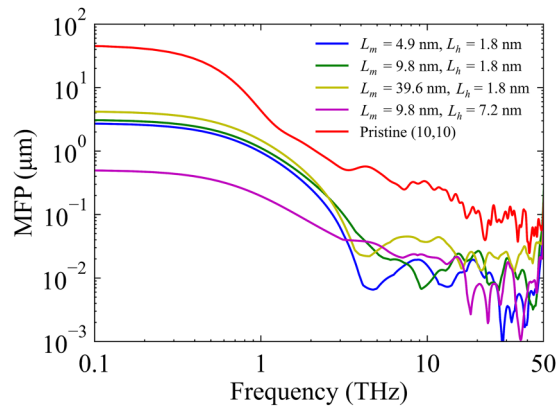


FIG. 4. Frequency-dependent phonon MFP in the (10,10)–(10,10) 1D branched CNT with different period L_m and branch height L_h .

for the modes in proximity to the flat bands, resulting in a decrease in group velocity.

To further analyze the transport properties of 1D CNTs with branches, we performed a spectral decomposition of the TC for (10,10)–(10,10) 1D branched structure. By applying Eq. (3), we further calculated the frequency-dependent phonon mean free path (MFP) and illustrated corresponding results in Fig. 4. In the pristine (10,10) CNT, the low-frequency phonon MFPs extend to tens of micrometers. As the frequency increases, the MFP gradually decreases and stabilizes around 100 nm above 20 THz. Introducing covalently bonded branched CNTs to the main CNT leads to a dramatic reduction in MFP across all frequencies. For instance, with $L_m = 4.9$ nm and $L_h = 1.8$ nm, the MFP is reduced by more than an order of magnitude across the entire frequency range. This reduction in MFP is more pronounced than that of phonon group velocity, suggests a simultaneous reduction of the phonon relaxation time. When the height of the branched CNT is fixed, the MFP increases as the period increases (corresponding to a decrease in branch density). More interestingly, at a fixed period, the phonon MFP sharply declines at low frequencies as the height of branched CNT increases from 1.8 to 7.2 nm, but remains almost unaltered at high frequencies. This behavior further indicates that the elongation of the branched CNT predominantly affects low-frequency phonons through the phonon resonance effect [44,46–48].

Covalently bonded CNT network structures have potential applications in heat-dissipation managements. To better understand the TC of CNT networks, we constructed 2D [Fig. 1(b)] and 3D [Fig. 1(c)] CNT network structures based on (10,10) CNTs and investigated their thermal-transport properties. Figure 5(a) illustrates the variation of TC with network periodicity, with a synchronized variation of periodicity in x , y , and z directions. It was observed that the TC of 3D networks is lower compared to that of 2D ones with the same periodicities. This discrepancy arises

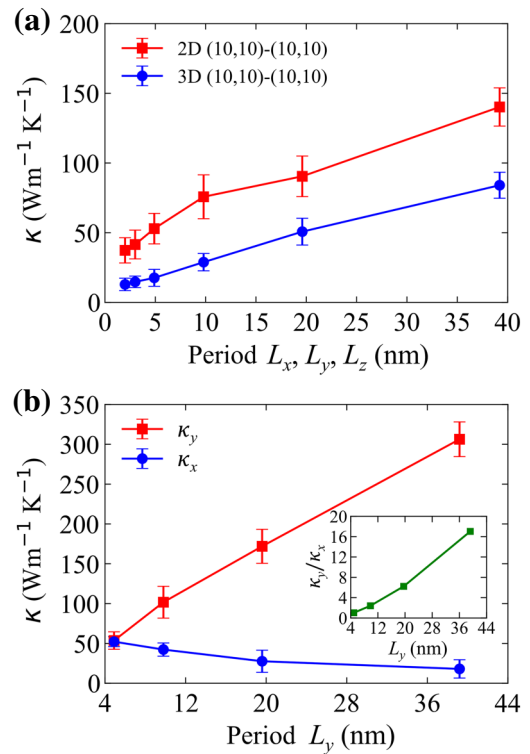


FIG. 5. (a) Variation of TC with period for 2D and 3D (10,10) CNT networks; (b) variation of TC along different directions with L_y in 2D (10,10) CNT networks, where L_x is fixed to 4.9 nm. The inset displays the variation of TC anisotropy ratio as a function of L_y .

due to the presence of additional cross-directional covalent bonds in the 3D structures, which leads to increased defect densities and amplified phonon-resonance effects. Although the TC of networked CNTs is considerably lower than that of pristine CNTs, the 3D structures maintain TCs exceeding $50 \text{ Wm}^{-1} \text{ K}^{-1}$ for periods beyond 20 nm, which is significantly superior to polymers [49]. Consequently, the covalently bonded CNT networks could be used as additives in thermal interface materials to improve the heat-dissipation ability by forming global heat-conductive networks. Similar to the 1D structures, the TC decreases as the period reduces, indicating that the structures with periods close to the CNT diameter exhibit the minimum TC. The smallest period we considered here is 2 nm for both 2D and 3D networks, with corresponding TCs of 37.3 and $12.9 \text{ Wm}^{-1} \text{ K}^{-1}$, respectively [Fig. 5(a)]. These values are close to the minimum TC of the corresponding systems as the period is only slightly larger than the diameter of CNTs (approximately 1.3 nm).

The above results demonstrate that the TC of CNT networks are highly dependent on the period length. To further probe the period dependence of TC in different directions, we changed the period along the y axis in a 2D CNT network while maintaining the period along

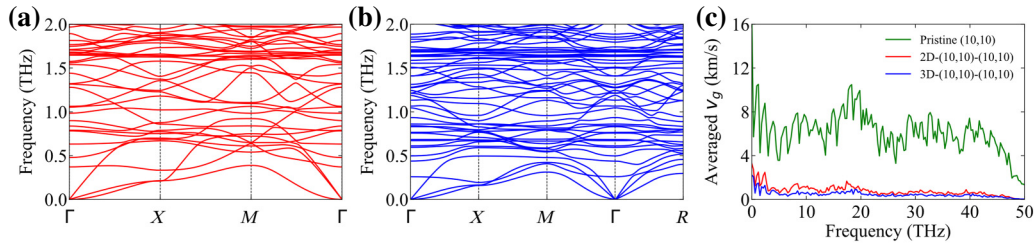


FIG. 6. Phonon dispersion relations of 2D (a) and 3D (b) (10,10) networked CNTs below 2 THz. The periods in both structures are set to 4.9 nm; (c) average phonon group velocity as a function of frequency for 2D and 3D (10,10) networked CNTs.

the x axis ($L_x = 4.9$ nm). Subsequently, the TCs along both the x and y directions were calculated and shown in Fig. 5(b). Interestingly, as L_y increases, the TC along the x axis and y axis exhibits a decreasing and an increasing trend, respectively. This phenomenon can be attributed to variations in defect density and resonant effect. With the increase of the period in the y direction, both the defect and side branch density along the y axis get reduced, leading to an increase of TC along this direction. Conversely, in the direction perpendicular to the y axis, the increase of L_y means the elongation of resonant branch, resulting in an enhanced resonant effect. Thus, the TC along the x direction is reduced, akin to the effects observed in 1D structures. The opposite trends of TCs along directions parallel and perpendicular to the period variation direction introduce anisotropic thermal transport within the CNT networks. Furthermore, it provides an effective way to tune the anisotropy ratio between different directions by increasing the period in one direction. For example, the TC ratio between κ_y and κ_x reaches 17 at $L_y = 39.6$ nm, demonstrating the tunability of anisotropy within the CNT networks [Fig. 5(b)].

Figures 6(a) and 6(b) depict the phonon-dispersion relations for both 2D and 3D CNT networks, where the period is set to 4.9 nm in all directions. Similar to the 1D case, numerous flat bands appear in the dispersion curves of both 2D and 3D network structures, indicating the presence of resonant phonons. These resonant phonons have a notable impact on thermal transport, leading to significant phonon softening and a substantial reduction in phonon group velocity, as shown in Fig. 6(c). The persistently lower group velocities observed throughout the entire frequency range in the 3D networks, compared to the 2D ones, imply a stronger resonant coupling effect in the former. This implies that the resonant phonons in the 3D networks have a more pronounced influence on phonon propagation, resulting in further reduction of the phonon group velocities.

Figure 7 shows the frequency-dependent phonon MFP within the 2D and 3D CNT networks. The MFP of the pristine (10,10) CNT is included for comparison purposes. As depicted in the figure, both the 2D and 3D CNT networks exhibit a significant reduction in phonon MFP across the

entire frequency range, similar to the behavior observed in the 1D case. Specifically, at frequencies below 1 THz, the MFP is reduced from tens of micrometers in the pristine CNT to a few microns in the 2D network. Besides, the MFP decreases further with a decrease in period length. Compared to the 2D case, the 3D CNT networks exhibit even smaller MFPs. For the investigated 3D structures, the phonon MFPs are all less than 1 μm and shrink to approximately 10 nm at high frequencies. Based on the aforementioned analysis, CNT network structures exhibit a combination of phonon scattering and resonant effects,

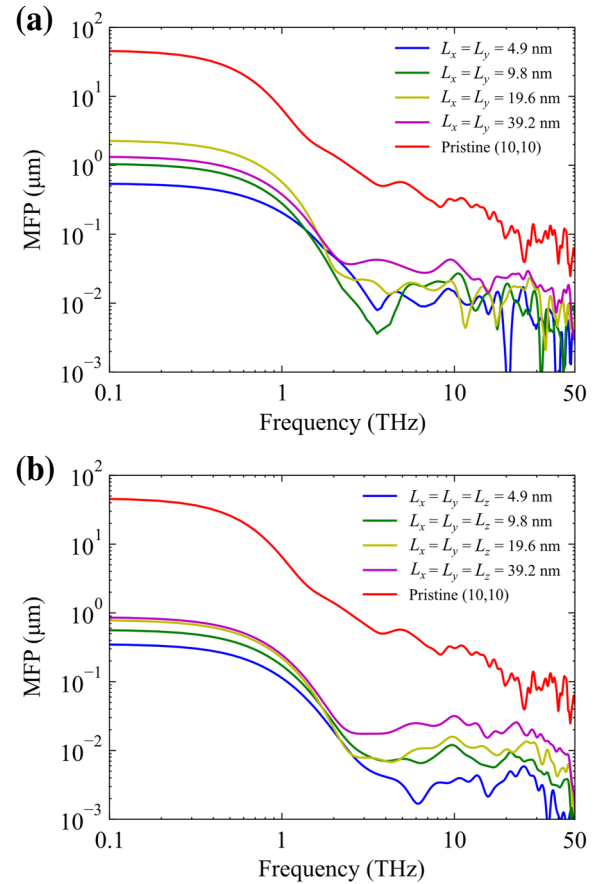


FIG. 7. Frequency-dependent phonon MFP for (a) 2D and (b) 3D (10,10) CNT network structures with different periods.

providing an efficient way to regulate phonon transport across the full frequency range. Consequently, these network structures hold potential applications in the design of structures with low TC, as they provide opportunities for effective regulation of phonon transport. In pristine CNTs, superdiffusive transport is observed at room temperatures [50]. In our covalently bonded CNT networks, we expect this superdiffusive transport to be suppressed due to the extensive resonant scattering of low-frequency phonons, which typically promotes superdiffusive transport.

IV. CONCLUSIONS

In this study, we have explored the thermal-transport properties of networked CNTs with covalent bonds by HNEMD simulations. Our results demonstrate a significant reduction in TC in networked CNT structures compared to the corresponding pristine CNTs. This reduction is primarily attributed to phonon scattering by defects at the junctions and the phonon-resonance effect generated by the CNTs perpendicular to the transport directions. At the junctions, defects introduce strong scattering of high-frequency phonons, while the phonon-resonant effect impedes the transport of low-frequency phonons. These combined effects lead to a significant reduction in TC. Additionally, the formation of defective carbon atomic rings at the junctions elevates the energy and stress levels of nearby atoms, which further disrupts the high-frequency phonon DOS. For structures ranging from 1D to 3D, an elongation of the network period leads to an increase of TC in the same direction while a decrease of TC in the perpendicular direction. This directional dependency is due to fewer defects and diminished resonant effect when the period is extended parallel to the transport direction, while the resonant effect is amplified with an increased period perpendicular to the transport direction. This observation provides an avenue for modulating the anisotropy of TC in networked CNTs, where the anisotropy ratio of TC intensifies with elongation of the period in a given direction. Our findings offer valuable insights into the mechanisms governing thermal transport in covalently networked CNTs and provide a foundational understanding for designing CNT-based structures for optimized thermal management applications.

ACKNOWLEDGMENTS

This work is supported by the National Natural Science Foundation of China (Grants No. 12174276 and No. 12304059), the Basic and Applied Basic Research Foundation of Guangdong Province (Grants No. 2024A1515010521 and No. 2022A1515110572).

- [1] D. Li, C. Wang, G. Sun, S. Senapati, and H.-C. Chang, A shear-enhanced CNT-assembly nanosensor platform for ultra-sensitive and selective protein detection, *Biosens. Bioelectron.* **97**, 143 (2017).
- [2] C. M. Hangarter, N. Chartuprayoon, S. C. Hernández, Y. Choa, and N. V. Myung, Hybridized conducting polymer chemiresistive nano-sensors, *Nano Today* **8**, 39 (2013).
- [3] J. Li, Y. Lu, Q. Ye, M. Cinke, J. Han, and M. Meyyappan, Carbon nanotube sensors for gas and organic vapor detection, *Nano Lett.* **3**, 929 (2003).
- [4] S. Park, M. Vosguerichian, and Z. Bao, A review of fabrication and applications of carbon nanotube film-based flexible electronics, *Nanoscale* **5**, 1727 (2013).
- [5] L. Wen, F. Li, and H.-M. Cheng, Carbon nanotubes and graphene for flexible electrochemical energy storage: From materials to devices, *Adv. Mater.* **28**, 4306 (2016).
- [6] W. Jian and D. Lau, Understanding the effect of functionalization in CNT-epoxy nanocomposite from molecular level, *Compos. Sci. Technol.* **191**, 108076 (2020).
- [7] V. D. Punetha, S. Rana, H. J. Yoo, A. Chaurasia, J. T. McLeskey, M. S. Ramasamy, N. G. Sahoo, and J. W. Cho, Functionalization of carbon nanomaterials for advanced polymer nanocomposites: A comparison study between CNT and graphene, *Prog. Polym. Sci.* **67**, 1 (2017). topical Volume on Nanocomposites.
- [8] H. Huang, C. Liu, Y. Wu, and S. Fan, Aligned carbon nanotube composite films for thermal management, *Adv. Mater.* **17**, 1652 (2005).
- [9] A. Liu, H. Xie, Z. Wu, and Y. Wang, Advances and outlook of TE-PCM system: A review, *Carbon Neutrality* **1**, 20 (2022).
- [10] C. Zhao, J. Yan, X. Tian, X. Xue, and Y. Zhao, Progress in thermal energy storage technologies for achieving carbon neutrality, *Carbon Neutrality* **2**, 10 (2023).
- [11] K. Kordás, G. Tóth, P. Moilanen, M. Kumpumäki, J. Vähäkangas, A. Uusimäki, R. Vajtai, and P. M. Ajayan, Chip cooling with integrated carbon nanotube microfin architectures, *Appl. Phys. Lett.* **90**, 123105 (2007).
- [12] S. Shenoy, J. Tullius, and Y. Bayazitoglu, Minichannels with carbon nanotube structured surfaces for cooling applications, *Int. J. Heat Mass Transf.* **54**, 5379 (2011).
- [13] Y. Fu, N. Nabiollahi, T. Wang, S. Wang, Z. Hu, B. Carlberg, Y. Zhang, X. Wang, and J. Liu, A complete carbon-nanotube-based on-chip cooling solution with very high heat dissipation capacity, *Nanotechnology* **23**, 045304 (2012).
- [14] G. Zhang and B. Li, Thermal conductivity of nanotubes revisited: Effects of chirality, isotope impurity, tube length, and temperature, *J. Chem. Phys.* **123**, 114714 (2005).
- [15] V. Datsyuk, S. Trotsenko, and S. Reich, Carbon-nanotube-polymer nanofibers with high thermal conductivity, *Carbon* **52**, 605 (2013).
- [16] H. Guo, J. Liu, Q. Wang, M. Liu, C. Du, B. Li, and L. Feng, High thermal conductive poly(vinylidene fluoride)-based composites with well-dispersed carbon nanotubes/graphene three-dimensional network structure via reduced interfacial thermal resistance, *Compos. Sci. Technol.* **181**, 107713 (2019).
- [17] W.-T. Hong and N.-H. Tai, Investigations on the thermal conductivity of composites reinforced with carbon nanotubes, *Diam. Relat. Mater.* **17**, 1577 (2008).

- [18] Y. Ni, H. Le Khanh, Y. Chalopin, J. Bai, P. Lebarry, L. Divay, and S. Volz, Highly efficient thermal glue for carbon nanotubes based on azide polymers, *Appl. Phys. Lett.* **100**, 193118 (2012).
- [19] J. Chen and J. Han, Effect of hydroxylated carbon nanotubes on the thermal and electrical properties of derived epoxy composite materials, *Results Phys.* **18**, 103246 (2020).
- [20] W. Tian, Y. Bao, G. Qin, L. Liu, and X. Zheng, Influence mechanism of functionalization of CNTs on the thermal transport property of their nanofluids, *J. Mol. Liq.* **392**, 123433 (2023).
- [21] Z. Yao, H. W. C. Postma, L. Balents, and C. Dekker, Carbon nanotube intramolecular junctions, *Nature* **402**, 273 (1999).
- [22] M. Fuhrer, J. Nygård, L. Shih, M. Forero, Y.-G. Yoon, M. Mazzoni, H. J. Choi, J. Ihm, S. G. Louie, A. Zettl *et al.*, Crossed nanotube junctions, *Science* **288**, 494 (2000).
- [23] M. Terrones, F. Banhart, N. Grobert, J.-C. Charlier, H. Terrones, and P. Ajayan, Molecular junctions by joining single-walled carbon nanotubes, *Phys. Rev. Lett.* **89**, 075505 (2002).
- [24] A. Krasheninnikov and F. Banhart, Engineering of nanostructured carbon materials with electron or ion beams, *Nat. Mater.* **6**, 723 (2007).
- [25] A. N. Andriotis, M. Menon, D. Srivastava, and L. Chernozatonskii, Rectification properties of carbon nanotube “ γ -junctions”, *Phys. Rev. Lett.* **87**, 066802 (2001).
- [26] A. Aiyiti, Z. Zhang, B. Chen, S. Hu, J. Chen, X. Xu, and B. Li, Thermal rectification in γ -junction carbon nanotube bundle, *Carbon* **140**, 673 (2018).
- [27] D. P. Hashim, N. T. Narayanan, J. M. Romo-Herrera, D. A. Cullen, M. G. Hahm, P. Lezzi, J. R. Suttle, D. Kelkhoff, E. Munoz-Sandoval, S. Ganguli *et al.*, Covalently bonded three-dimensional carbon nanotube solids via boron induced nanojunctions, *Sci. Rep.* **2**, 363 (2012).
- [28] E. Tylianakis, G. K. Dimitrakakis, S. Melchor, J. A. Dobado, and G. E. Froudakis, Porous nanotube network: A novel 3-D nanostructured material with enhanced hydrogen storage capacity, *Chem. Commun.* **47**, 2303 (2011).
- [29] C. Klinke, J. Chen, A. Afzali, and P. Avouris, Charge transfer induced polarity switching in carbon nanotube transistors, *Nano Lett.* **5**, 555 (2005).
- [30] M. Haselman and S. Hauck, The future of integrated circuits: A survey of nanoelectronics, *Proc. IEEE* **98**, 11 (2010).
- [31] V. Varshney, A. K. Roy, G. Froudakis, and B. L. Farmer, Molecular dynamics simulations of thermal transport in porous nanotube network structures, *Nanoscale* **3**, 3679 (2011).
- [32] S. Nakarmi, V. U. Unnikrishnan, V. Varshney, and A. K. Roy, Multi-terminal nanotube junctions: Modeling and structure-property relationship, *Front. Mater.* **8**, 692988 (2021).
- [33] Z. Fan, W. Chen, V. Vierimaa, and A. Harju, Efficient molecular dynamics simulations with many-body potentials on graphics processing units, *Comput. Phys. Commun.* **218**, 10 (2017).
- [34] J. Tersoff, Modeling solid-state chemistry: Interatomic potentials for multicomponent systems, *Phys. Rev. B* **39**, 5566 (1989).
- [35] Z. Fan, H. Dong, A. Harju, and T. Ala-Nissila, Homogeneous nonequilibrium molecular dynamics method for heat transport and spectral decomposition with many-body potentials, *Phys. Rev. B* **99**, 064308 (2019).
- [36] G. J. Martyna, M. L. Klein, and M. Tuckerman, Nosé–Hoover chains: The canonical ensemble via continuous dynamics, *J. Chem. Phys.* **97**, 2635 (1992).
- [37] Y. Zhou and M. Hu, Quantitatively analyzing phonon spectral contribution of thermal conductivity based on nonequilibrium molecular dynamics simulations. II. From time Fourier transform, *Phys. Rev. B* **92**, 195205 (2015).
- [38] K. Sääskilähti, J. Oksanen, S. Volz, and J. Tulkki, Frequency-dependent phonon mean free path in carbon nanotubes from nonequilibrium molecular dynamics, *Phys. Rev. B* **91**, 115426 (2015).
- [39] Z. Fan, L. F. C. Pereira, P. Hirvonen, M. M. Ervasti, K. R. Elder, D. Donadio, T. Ala-Nissila, and A. Harju, Thermal conductivity decomposition in two-dimensional materials: Application to graphene, *Phys. Rev. B* **95**, 144309 (2017).
- [40] X. Gu, Z. Fan, and H. Bao, Thermal conductivity prediction by atomistic simulation methods: Recent advances and detailed comparison, *J. Appl. Phys.* **130**, 210902 (2021).
- [41] C. Sevik, H. Sevinçli, G. Cuniberti, and T. Çağm, Phonon engineering in carbon nanotubes by controlling defect concentration, *Nano Lett.* **11**, 4971 (2011).
- [42] J. Yang, W. Zhang, S. Q. Bai, Z. Mei, and L. D. Chen, Dual-frequency resonant phonon scattering in $\text{Ba}_x\text{RyCo}_4\text{Sb}_{12}$ ($R = \text{La, Ce, and Sr}$), *Appl. Phys. Lett.* **90**, 192111 (2007).
- [43] B. Dongre, J. Carrete, A. Katre, N. Mingo, and G. K. H. Madsen, Resonant phonon scattering in semiconductors, *J. Mater. Chem. C* **6**, 4691 (2018).
- [44] S. Xiong, K. Sääskilähti, Y. A. Kosevich, H. Han, D. Donadio, and S. Volz, Blocking phonon transport by structural resonances in alloy-based nanophononic metamaterials leads to ultralow thermal conductivity, *Phys. Rev. Lett.* **117**, 025503 (2016).
- [45] J. D. Gale and A. L. Rohl, The general utility lattice program (GULP), *Mol. Simul.* **29**, 291 (2003).
- [46] J. Chen, J. He, D. Pan, X. Wang, N. Yang, J. Zhu, S. A. Yang, and G. Zhang, Emerging theory and phenomena in thermal conduction: A selective review, *Sci. China Phys., Mech. Astron.* **65**, 117002 (2022).
- [47] X. Wan, D. Ma, D. Pan, L. Yang, and N. Yang, Optimizing thermal transport in graphene nanoribbon based on phonon resonance hybridization, *Mater. Today Phys.* **20**, 100445 (2021).
- [48] D. Ma, H. Ding, H. Meng, L. Feng, Y. Wu, J. Shiomi, and N. Yang, Nano-cross-junction effect on phonon transport in silicon nanowire cages, *Phys. Rev. B* **94**, 165434 (2016).
- [49] X. Xu, J. Chen, J. Zhou, and B. Li, Thermal conductivity of polymers and their nanocomposites, *Adv. Mater.* **30**, 1705544 (2018).
- [50] G. Zhang and B. Li, Anomalous vibrational energy diffusion in carbon nanotubes, *J. Chem. Phys.* **123**, 014705 (2005).